JOURNAL OF AIRCRAFT
Vol. 29, No. 3, May–June 1992

Application of Active Flexible Wing Technology to the Agile Falcon

Edmund Pendleton* and Mark Lee*
Wright Laboratory, Wright-Patterson Air Force Base, Ohio 45433
and
Lee Wasserman†
Delta Dynamics, Inc., Dayton, Ohio 45432

The Active Flexible Wing is an integrated technology wing concept of special interest to systems requiring high maneuverability at high speed. The following article examines the results from an application of the Active Flexible Wing (AFW) concept to an F-16 Agile Falcon, low-speed aeroelastic model. The article also summarizes, for archival purposes, design and fabrication procedures typical for construction of low-speed aeroelastic models. The Active Flexible Wing concept is applied to a $\frac{1}{5}$ scale model design based upon full scale preliminary wing design studies conducted for the U.S. Air Force F-16 Agile Falcon fighter program. The model is equipped with multiple leading- and trailing-edge control surfaces. Wind tunnel test results are presented showing wing control power increases generated through the use of the leading- and trailing-edge control surfaces in conjunction with increased wing flexibility. The results show that the Active Flexible Wing concept is a viable concept for the Agile Falcon planform and that a leading-edge outboard control surface can be a particularly powerful control power effector.

Introduction

ADVANCES in metallic and composite structure technologies, high-authority automatic flight control systems, and enhanced design techniques have resulted in modern aircraft that are increasingly responsive and have greater structural efficiency. Many of these advances in structural dynamics, flight controls, and aerodynamics have evolved independently. However, full benefit of these advances is achieved when the technologies function in concert. In addition, aircraft design trends have emerged that point to vehicles of the future that are increasingly flexible, emphasizing the need to integrate structures and flight controls at the onset of the design process.

One integrated technology wing concept, of special interest to systems requiring high maneuverability at high speed, is the Active Flexible Wing.[1] Initially developed from 1983 to 1987 under an Air Force contract with Rockwell International, this concept represents a return to the Wright Brothers' idea of wing warping or twisting by combining wing structures and flight controls to produce an integrated configuration with superior performance.

A key aspect of the AFW concept is the use of multiple leading- and trailing-edge control surfaces on a flexible wing. Wing control power, which traditionally is diminished at high dynamic pressures where trailing-edge control surfaces become ineffective due to wing aeroelastic twist, is maintained by scheduling leading- and trailing-edge surfaces such that the wing is deformed to provide the greatest amount of control power possible. At high dynamic pressures, control surfaces are used not as primary control force-producing devices, but as aerodynamic tabs that aeroelastically twist the wing to produce beneficial wing deformations. The total wing deformations produce the control forces. Leading-edge control surfaces produce increased deformation and become more effective with increases in dynamic pressure. Trailing-edge surfaces are deflected such that the moments produced also deform the wing to provide additional control power. Control surface deflections are optimized as a set to produce the most efficient control at a given flight condition. An active control system is used to provide gain scheduled control surface deflections throughout the entire range of Mach numbers and dynamic pressures to provide a fighter more control power to perform a desired maneuver (such as roll).

To examine some of the benefits attainable through incorporating the AFW concept on an operational Air Force fighter and to verify trends from previous efforts, the Flight Dynamics Laboratory initiated an in-house aeroelastic model test program. The objective of this project was to investigate experimentally the effects of reduced wing stiffness on wing roll control power and to demonstrate the use of multiple leading- and trailing-edge control surfaces on an F-16 derivative planform. Currently, the F-16 fighter uses a differential tail to aid the wing during rolling maneuvers at high dynamic pressures. AFW technology offers a potential alternative solution to the use of a rolling tail.

A low-speed aeroelastic model[2] was designed and fabricated based upon preliminary wing design studies conducted in conjunction with a proposed wing upgrade for the U.S. Air Force F-16 fighter. The baseline low-speed model was designed based upon mass, stiffness, and planform data present in an MSC NASTRAN[3,4] finite element model. Multiple leading- and trailing-edge control surfaces were provided by adding an outboard trailing-edge control surface and segmenting the leading-edge control surface. A second wing box spar, where the outboard stiffness was reduced from the baseline, was constructed to demonstrate the use of the AFW concept. The model was equipped with interchangeable actuators so that control surface settings could be manually set and flexible lift and roll derivatives could be obtained.

Results from the design, fabrication, and wind-tunnel tests are presented as well as correlation with the Automated Structural Optimization System (ASTROS) computer code.[5,6] Wind tunnel test data presented verify that increases in wing flex-

Received Dec. 1, 1990; presented as Paper 91-0987 at the AIAA/ASME/ASCE/AHS/ASC Structures, Structural Dynamics, and Materials Conference, Baltimore, MD, April 8–10, 1991; revision received May 13, 1991; accepted for publication May 17, 1991. This paper is declared a work of the U.S. Government and is not subject to copyright protection in the United States.

*Aerospace Engineer, Flight Dynamics Laboratory.
†Aerospace Engineering Consultant, 3813 Knollwood Drive.

ibility can enhance leading-edge control power and more uniformly distribute control power across the flight envelope, resulting in substantial increases in wing control power over that attained from the baseline design.

Low-Speed Model Design

The primary objective of the baseline aeroelastic model design was to simulate, with reasonable accuracy, a full-scale composite wing preliminary design proposed for the F-16 Agile Falcon. The baseline model was scaled from design data presented in an MSC NASTRAN finite element model. Figure 1 depicts the full-scale planform and the spar and material arrangement.

A major design constraint required the model to be constructed in a low-cost, timely manner. Therefore, the design procedure selected relied on an approach typical of low-speed models where aluminum spars, simulating the wings's elastic forces, were used to support a set of spanwise airfoil sections constructed of aluminum reinforced balsa with ballast weights. The balsa formed the contour to provide proper aerodynamic forces and, in combination with ballast weights, provided the proper inertial forces.

The model was scaled for tests in the Air Force Institute of Technology's (AFIT) subsonic 5-ft wind tunnel. Based on a two-dimensional analysis using the aerodynamics from Ref. 7, a velocity ratio was chosen so the baseline model trailing-edge outboard (TEO) surface was at the point of "aeroelastic reversal" near the top of the wind-tunnel envelope. The geometric scale factor was chosen to reduce the 183.5 inch, full-scale semispan wing to fit in a 5-ft diam tunnel. Table 1 lists model scale factors, including units for converting from full-scale mass in pounds to model-scale in grams and full-scale stiffness to model-scale stiffness in pounds and inches.

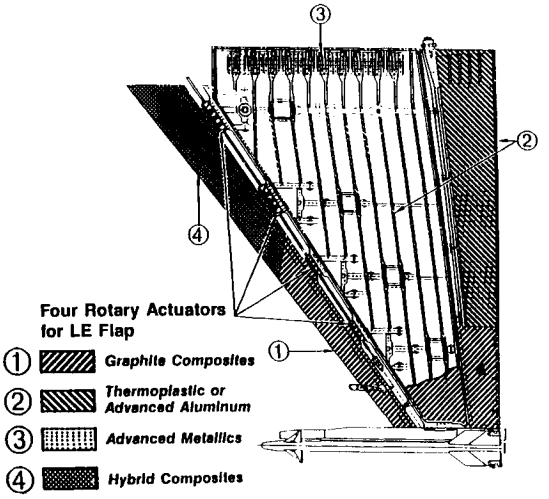

Fig. 1 Full-scale spar and material arrangement.

Table 1 Scale factors for low-speed model

Parameter	Scale factor	Units
Geometric	0.200	
Velocity	0.152	
Density	1.00	
Dynamic pressure	0.023	
$v/b\omega$	1.0	
Frequency (ω)	0.76	
	Mass properties	
Mass	3.6320	g/lb
Unbalance	0.72640	g in./lb in.
Inertia	0.14528	g in./lb in.^{2}
	Stiffness properties	
k	4.62 E-3	lb/in.
EI	3.69 E-5	lb in.^{2}
GJ	3.69 E-5	lb in.^{2}

The model was designed to be constructed in spanwise sections to minimize the amount of bending and torsional stiffness contributed to the model by the aerodynamic sleeve. The wing box consisted of nine aluminum-reinforced balsa sections, and the leading- and trailing-edge control surfaces each consisted of nine aluminum-reinforced balsa sections.

The wing sections were attached to a wing box spar and control surface sections were attached to four separate control surface spars. Springs, simulating both actuators and hinges, were used to attach each of the control surface spars to the wing box sections. Each of the balsa sections was mass balanced so that mass, static unbalance, and mass moment of inertia properties corresponded to full-scale values. Figure 2 shows the section layout of the scaled aeroelastic model.

Model geometry was scaled to be identical to the full-scale preliminary design. Full-span wing aspect ratio was 3.75, the taper ratio based on tip and fuselage centerline chords, 0.218, and the thickness to chord ratio, 3.8%. The leading-edge sweep was 34.3 deg aft and the trailing-edge was unswept.

Airfoil selection was based on full-scale specifications, but was modified to simplify both model fabrication and model trim in the tunnel. A symmetric, 3.8% thick, NACA 64A series airfoil section without twist was incorporated along the entire wing span because airfoil camber and twist do not affect results obtained with low-speed flutter models.

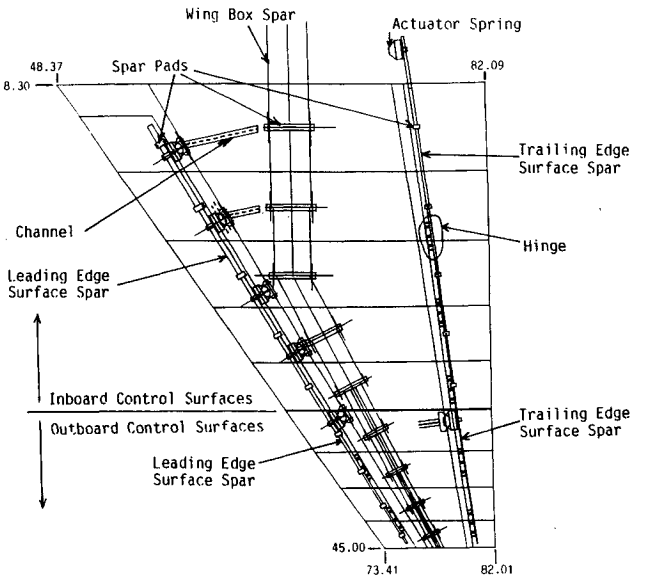

Fig. 2 Aeroelastic model layout-spars, actuators, and hinge attachments.

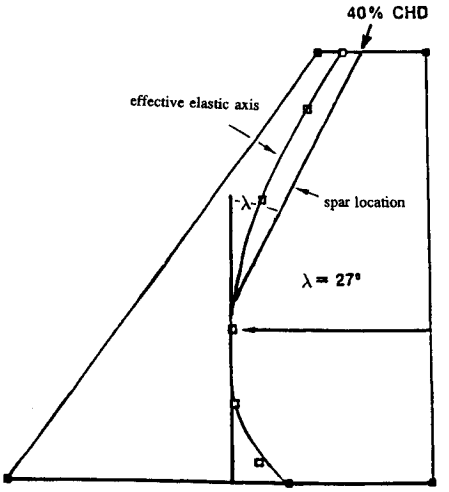

Fig. 3 Location of effective elastic axis.

Wing Box Stiffness

A key to this design procedure is placement of the model wing spar as near the elastic axis as possible. The elastic axis is represented by the locus of shear centers of the cross sections of the wing. The shear center of each airfoil cross section is determined to be the point in the plane of the section where a shear force can be applied to the section without producing a twist.[8] The full-scale wing's effective elastic axis was found by computing the chordwise points of zero deflection from influence coefficients for a pitching moment applied at the wing tip. The effective elastic axis approximates the true elastic axis location when the elastic axis is parallel to the pitching axis. For a swept elastic axis, the pitching moment causes some wing bending, which shifts the effective elastic axis forward, as shown in Fig. 3. The set of influence coefficients was generated using the full-scale NASTRAN finite element model. Bending (EI) and torsional (GJ) stiffnesses were determined using the cantilever beam equations. Figure 4 shows the scaled stiffness distributions along the wing box determined from the finite element model.

The kinked beam spar design, shown in the layout in Fig. 2, was selected to model the wing box stiffness. NASTRAN analyses indicated that this spar design deformed with deflection and bend/twist characteristics that approximate the influence coefficient description. More precision in matching the influence coefficient description might have been attained through design of a more complicated and costly structure. However, past experiences in the construction of low-speed aeroelastic models has shown that the simulation of actual aircraft structures by beams located on the elastic axis will give acceptable results.

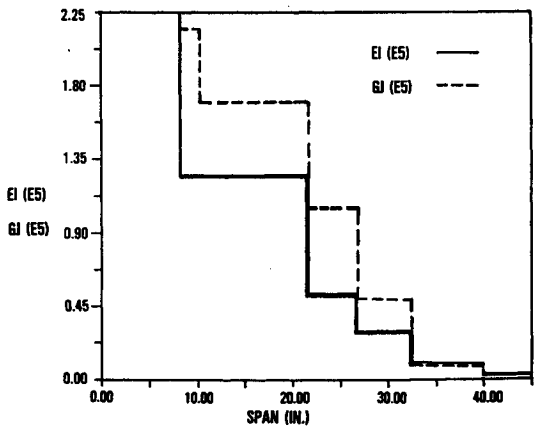

Fig. 4 Baseline wing-box stiffness distribution.

The kinked wing spar was designed to be constructed of aluminum with a flanged rectangular cross section with width and thickness reductions at successive outboard stations. Values for bending inertia I_a and torsion inertia J were modeled by selecting appropriate widths and thicknesses according to formulas listed in Ref. 9. A fore and aft flange was added to the outboard portion of the kinked spar to maintain chordwise fore and aft stiffness EI_b at least ten times the sectional bending stiffness EI_a. Built-up aluminum pads were provided at aerodynamic section attachment points so minimal section stiffness was transferred to the spar. Table 2 depicts target spanwise bending and torsional slopes due to a unit load and moment at the wing tip and values of I_a, J, and J/I_a ratio for the main spar.

A second wing box spar was designed to be identical to the first, but the bending and torsional stiffness outboard of the spar kink angle reduced to 75% of the baseline wing spar. The global wing stiffness was not reduced due to flutter considerations, and because scaling laws can be used to derive reasonable estimates of control power output from baseline data. When incorporated into the model, this reduced stiffness spar provided the increase in wing flexibility necessary for an investigation and verification of the AFW concept.

Control Surface Stiffness

Four control surface spars were designed to model control surface stiffness. Each spar's torsional stiffness characteristics were modeled by designing the aluminum spar with a square cross section with reductions in thickness at successive stations.

Full-scale control surface torsional stiffnesses for the leading-edge surfaces and the trailing-edge inboard surface were determined in a manner similar to the wing box spar. Stiffness values for the trailing-edge outboard surface were extrapolated based on inboard surface stiffness data. Scaled torsional stiffnesses were required to accurately simulate control surface frequency response, static wind up, and effect on flutter. Full-scale bending stiffnesses were not modeled. Control surface bending strength, which had to withstand significant airloads (approximately 0.5 psi), was verified by loading the surface with a distributed load equivalent to 1.5 psi.

A tapered flange was added to each control surface spar to provide adequate fore and aft stiffness. Similar to the wing box, built-up aluminum pads were located at each section midstation so that a set of aluminum reinforced balsa airfoil sections could be attached with minimal stiffness transfer to the model. Actuator attachment pads were also machined into each spar at the actuator attachment points.

Table 2 Model wing box target inertia properties

Full-scale span station	Model span station	Bending slope (model)	Torsion θ (model)	I_a (E-3) Target (model), in.^{4}	J (E-3) Target (model), in.^{4}	J/I_a Target (model)
58.5	11.7	0.27087E-04	0.17419E-04			
				11.8	42.5	3.6
89.80	17.96	0.76959E-04	0.53690E-04			
				8.16	35.5	4.4
116.6	23.32	0.13894E-03	0.90830E-04			
				3.53	17.1	4.8
140.0	28.0	0.26414E-03	0.15819E-03			
				2.46	10.8	4.4
160.45	32.09	0.42112E-03	0.25178E-03			
				0.938	2.18	2.3
178.35	35.67	0.78106E-03	0.65665E-03			
				0.886	2.02	2.3
193.95	38.79	0.11132E-02	0.10362E-02			
				0.290	0.802	2.8
207.55	41.51	0.19989E-02	0.18708E-02			
				0.203	0.582	2.9
219.45	43.89	0.31019E-02	0.28782E-02			

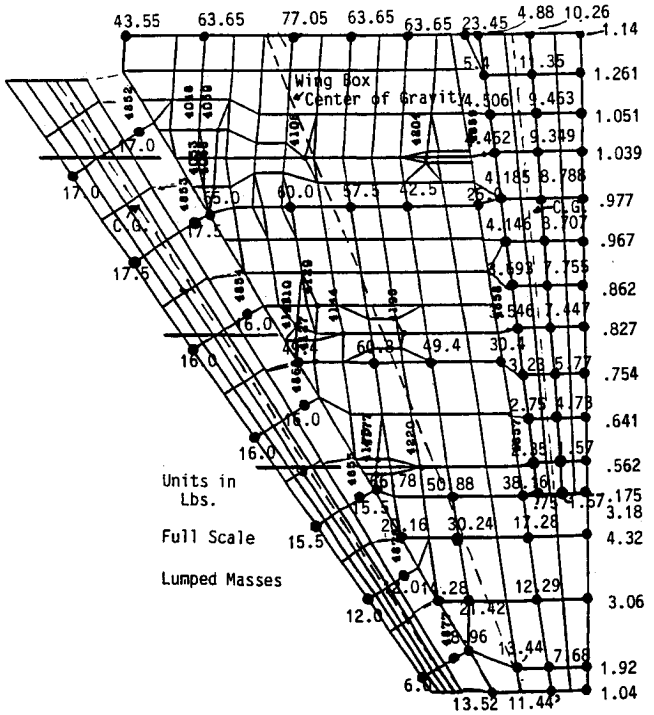

Fig. 5 NASTRAN full-scale mass distribution.

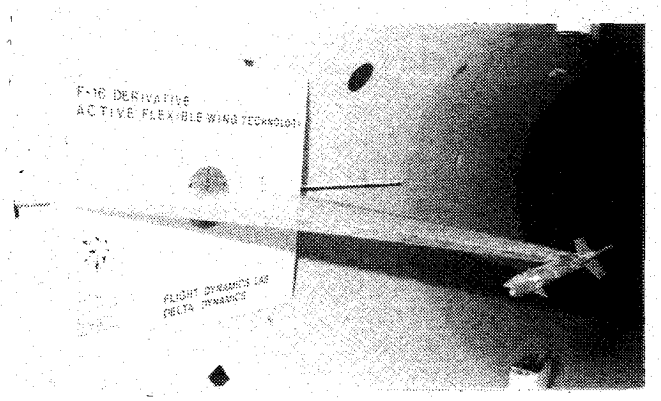

Fig. 6 Baseline, $\frac{1}{3}$ scale, low-speed flexible model.

Mass Properties

Wing full-scale mass properties were simulated based upon the lumped masses given at specified spanwise locations in the NASTRAN finite element model. These are depicted in Fig. 5. These masses were used to determine the wing section chordwise target values for mass, static unbalance, and mass moment of inertia. Target mass and moment of inertia values for the model wing box are presented in Table 3.

Actuator and Hinge Modeling

Full-scale actuator stiffness values were simulated by springs in the form of aluminum brackets that connected the control surface spars to the wing box. Four actuators connected the inboard leading-edge surface. The outboard surface was connected with one leading-edge actuator and two hinge points. Because the leading- and trailing-edge surfaces were segmented, a trailing-edge outboard actuator was added to the outboard flaperon. In addition to this actuator, the outboard trailing-edge control surface was connected at two hinge points. The inboard trailing-edge surface was connected by one actuator and three hinges. Figure 2 depicts the master layout containing the location of all the spars, actuators, and hinges.

Hinges were constructed of springs with low rotational stiffness to reduce the damping normally encountered with ball

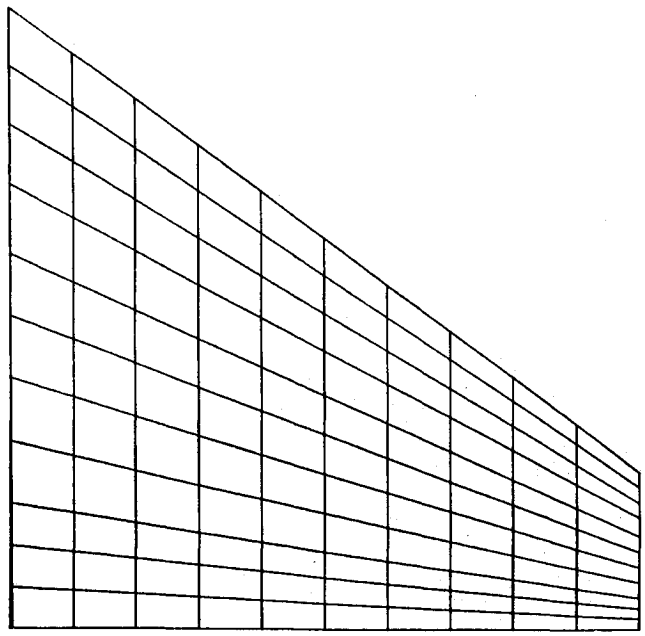

Fig. 7 Doublet-lattice aerodynamic box pattern.

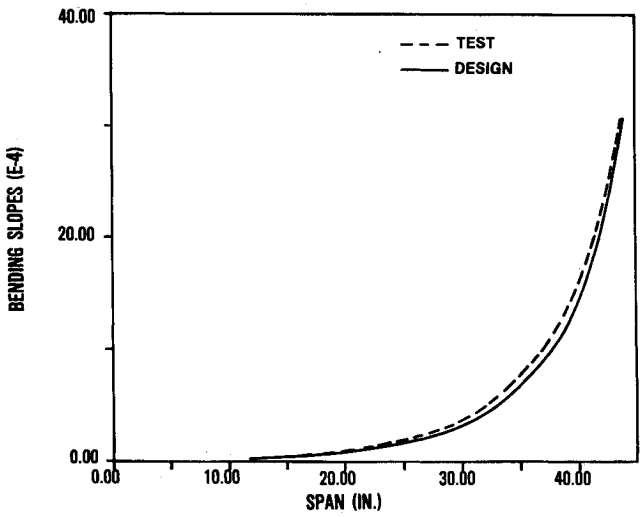

Fig. 8 Spanwise bending slope comparison due to a unit load.

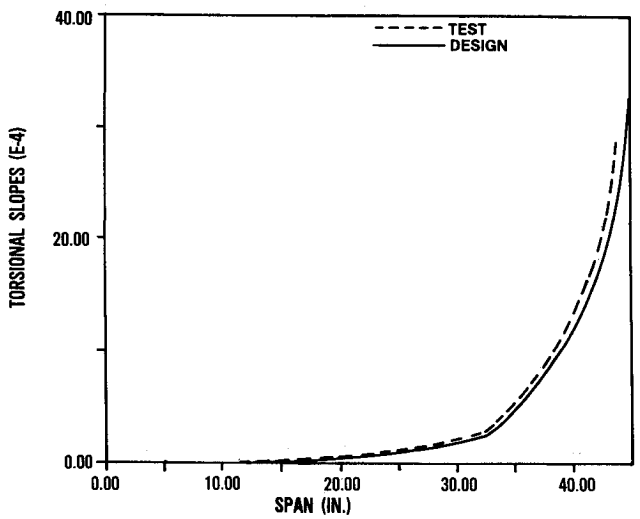

Fig. 9 Spanwise twist slope comparison due to a unit moment.

bearing hinges. Each hinge consisted of a 1.5-in. piece of angled beryllium copper, which was connected to three small steel attachment fittings. The two outside attachment fittings connected the control surface spar to the spring hinge, and the center attachment connected the hinge to the wing box section.

AIM-9 Missile and Hardpoint Provisions

Aluminum pads were designed and constructed along the wing spar oriented along the flow direction at full-scale store hardpoint locations. These pads permitted the addition of inboard pylons for store attachment. A model AIM-9 (Sidewinder) missile, launcher, and associated rigid attachment were fabricated and mass-balanced so that tip store effects could be evaluated.

Model Fabrication

The goal during fabrication was to simulate scaled deflection and modal response characteristics of the full-scale design closely. Measured stiffness distributions for each spar were required to approximate target values closely. Measured section mass and inertia properties were required to fall within 10% of design values, and centers of gravity within 5% of the chord. In addition, the model had to have sufficient strength to accept test section airloads and have the correct geometric shape and airfoil contour.

Final mass balance measurements showed the total wing mass matched the finite element model requirement within 0.3%. Wing box mass matched scaled aircraft requirements within 3%. Control surface mass values were 8% under target for the leading-edge surfaces and 18% under the trailing-edge surfaces. The average static unbalance was 20% under target for the trailing-edge flap. The low mass values are the likely cause of the slightly high flap frequencies noted during modal testing.

Because the aerodynamic sleeve was sectioned, airgaps were created between each of the wing box and control surface sections. Foam rubber was used to seal the wing box section

Table 3 Model wing box target mass properties

Model air gaps, in.	Model midsta., in.	Width, in.	Mass, g	Midsta. chord (LE to TE)	I, g/in.^{2}	Max. thick., in.	Box chord (hinge-to-hinge)
8.30			[a]751.8				
	11.7	6.8	708.2	31.39	22111.0	1.19	21.02
15.10							
	17.96	5.72	566.6	27.11	13189.0	1.03	16.91
20.82							
	23.32	5.0	475.8	23.44	8280.0	0.892	14.41
25.82							
	28.00	4.36	395.9	20.23	5135.0	0.770	12.23
30.18			[a]148.9				
	32.09	3.82	335.6	17.44	3232.0	0.665	10.30
34.00							
	35.67	3.34	278.9	14.98	1984.0	0.572	8.7
37.34							
	38.79	2.9	152.9	12.85	800.0	0.491	7.3
40.24							
	41.51	2.54	98.8	10.99	378.0	0.421	5.98
42.78							
	43.89	2.22	59.7	9.36	166.0	0.359	4.88
45.00							

[a]Residual Masses added to sections 1 and 5.

Table 4 Baseline model natural frequencies

Mode	F.E.M. Full-scale aircraft, Hz	F.E.M. Model-scale target, Hz	Measured model (sine dwell), Hz	Measured model (random), Hz	ASTROS model, Hz
1st bending	7.25	5.5	5.6	5.6	5.6
TEI flaperon	20.4	15.5	17.6	17.6	17.6
2nd bending	25.3	19.2	20.6	20.4	17.4
1st torsion	33.5	25.5	28.8	29.1	26.9
TEI bending	41.4	31.5	33.8	34.4	33.7
2nd torsion	58.9	44.8	41.3	41.1	37.3
Higher	47.6	36.2	[a]	[a]	33.6
Composite	51.8	39.4	[a]	[a]	[a]
Wing Modes—					
3rd bending	63.9	48.6	45.7	46.8	42.5

(Clean wing, no launcher/missile attached.)
[a]Undetermined.

1st bending	4.1	3.1	3.3	3.3	3.3
Missile pitch	6.4	4.9	6.3	6.3	5.3
2nd bending	15.2	11.6	11.8	11.9	11.8
TEI flaperon	22.1	16.7	19.8	19.5	17.5
1st torsion	35.0	26.6	27.4	27.7	25.4
TEI bending	[a]	[a]	33.7	34.0	33.7
3rd bending	[a]	[a]	35.3	36.2	33.4

(Launcher/missile attached.)
[a]Undetermined.

Table 5 Reduced stiffness model natural frequencies

Mode	Measured model (sine dwell), Hz	Measured model random, Hz	ASTROS model, Hz
1st bending	5.6	5.6	5.3
2nd bending	17.3	17.3	16.3
TEI flaperon	21.8	22.3	17.5
1st torsion	28.4	28.5	25.3
TEI bending	36.3	39.6	33.6
2nd torsion	40.3	[a]	34.7
3rd bending	46.3	45.1	40.6
(Clean wing, no launcher/missile attached.)			
1st bending	3.1	3.1	3.1
Missile pitch	5.7	5.9	4.9
2nd bending	11.3	11.2	12.1
TEI flaperon	21.7	[a]	17.5
1st torsion	26.4	26.7	26.1
TEI bending	37.0	37.2	33.6
3rd bending	33.9	34.4	34.8
(Launcher/missile attached.)			

[a]Undetermined.

airgaps. The airgap dimensions between the control surface sections were minimized, but left unsealed because the foam increased stiffness slightly. Figure 6 shows the finished model cantilevered to a splitter plate mounted in the AFIT 5-ft tunnel.

ASTROS Analyses

An ASTROS finite element mathematical model was prepared using model design stiffness and measured mass data. The model consisted of beam elements, scalar elastic elements, and lumped masses. The finite element model was used to predict load deflections and to perform vibration and flutter analyses. Doublet Lattice[10] aerodynamics were used for flutter predictions.

Flexible wing rolling effectiveness predictions were performed as well as wing stiffness-aileron effectiveness trend studies to determine stiffness values for reducing the wing box spar stiffness. The USSAERO aerodynamic routine in ASTROS was used for steady aerodynamics. Because the splitter plate represents a symmetrical aerodynamic boundary condition, the analyses may be used to predict test results for this condition and the change due to an antisymmetrical condition. Figure 7 shows the aerodynamic box pattern used for steady aerodynamics.

Ground Tests

Load Tests

Stiffness tests on the wing box spar showed excellent correlation between target and measured bending (EI) and torsional (GJ) stiffnesses. Measured deflections along the spar agreed closely with ASTROS static analyses of the spar. Outboard deflection measurements at influence coefficient locations also agreed reasonably with scaled deflections from outboard influence coefficient locations in the full-scale NASTRAN finite element model. Figures 8 and 9 depict measured bending and torsional slope deflections due to a unit load and moment applied at the wing tip respectively and comparison with model design targets. Model strength was tested by loading the wing with a distributed load of 1.5 psi. This loading was approximately three times the maximum wind tunnel dynamic pressure.

Vibration Tests

A vibration survey was conducted on the model using random and sine dwell techniques to determine modal characteristics. A 2-lb vibration shaker was used to excite the wing

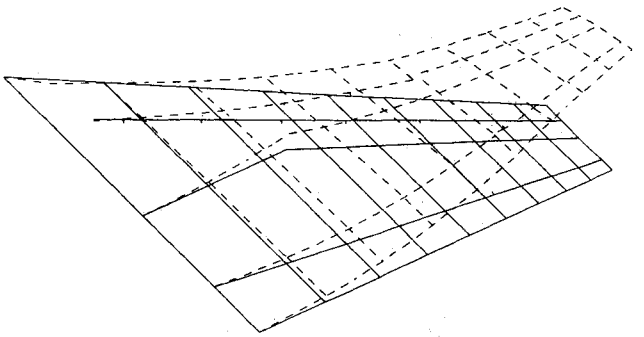

Fig. 10 Baseline wing—1st bending mode.

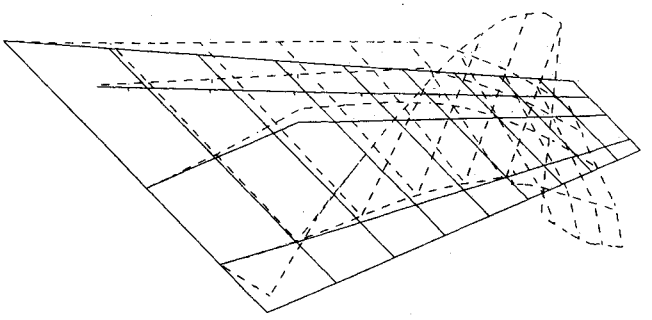

Fig. 11 Baseline wing—1st flaperon mode.

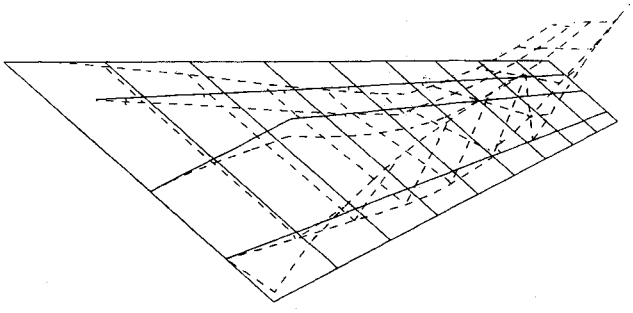

Fig. 12 Baseline wing—2nd bending mode.

natural frequencies. Optimum excitation locations were evaluated by placing the shaker at various locations on the wing. Following shaker attachment at a location slightly inboard along the wing box trailing edge, the model was excited using a random source. Wing acceleration was measured for each of four configurations at selected wing locations using a random vibration measurement system. Supplementary measurements were also made with the shaker located outboard along the wing box leading edge.

Following the random survey, each natural mode was found by exciting the wing at its natural frequency. Accelerometer measurements were made at various locations on the wing surface to tune natural frequencies and identify node lines and phasing relationships.

Measured mode shapes and frequencies of the baseline model were compared to the two sets of predicted mode shapes and frequencies, the set generated using the full-scale NASTRAN finite element model, and the set ASTROS generated using the $\frac{1}{3}$ scale aeroelastic finite element model. Qualitative comparisons, using the mode shapes' relative amplitudes, nodes, and phasing showed good agreement for each of the five wing modes. Natural frequency comparison between the model and scaled aircraft design values for the first four wing modes differed 0%, 4%, 8%, and 9%, respectively. The model's trailing-edge inboard (TEI) flaperon modes were 13% higher than aircraft design values. The slightly high, measured flaperon frequency was not adjusted further because the primary application for these tests of the model was static aeroelastic investigations. Tables 4 and 5 show natural frequency com-

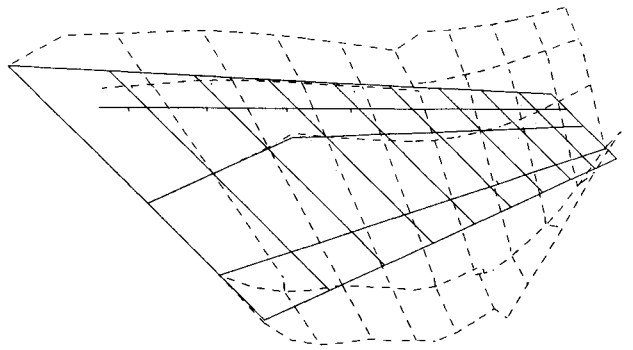

Fig. 13 Baseline wing—1st torsion mode.

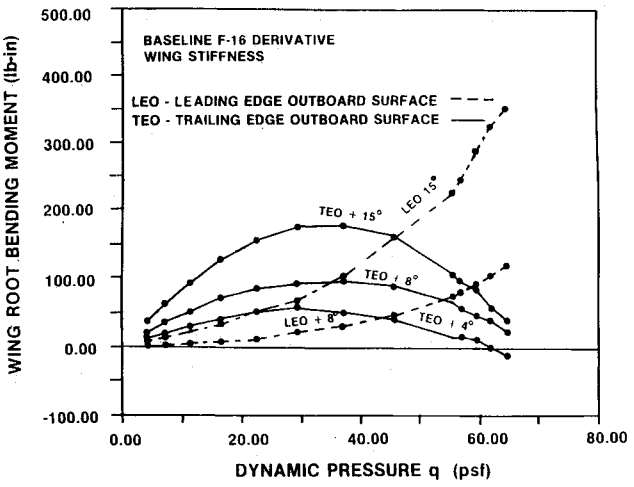

Fig. 14 Baseline wing root bending moments due to outboard surface deflection.

parisons for the baseline and reduced stiffness models. Figures 10 through 13 show the finite element representation and the baseline model mode shapes for the wing first bending, flaperon, second bending, and first torsion modes.

Wind-Tunnel Results

Wind-tunnel testing began by mounting the splitter plate to the side of the 5-ft tunnel. The splitter plate was equipped with a rotatable disk to provide adjustments in model angle of attack.

Both configurations, the model with the baseline F-16 derivative spar installed and the model with the reduced stiffness spar installed, were tested. Strain gauges, mounted on the wing box spar at the wing root, provided wing bending and torsional moment measurements as dynamic pressure and control surface setting were varied. Wing root bending moment, which is directly proportional to aircraft rolling moment, was of primary interest.

A flutter clearance run for the clean wing, baseline model was conducted to a dynamic pressure of 78 psf. This run verified the absence of dynamic instabilities for this configuration within the tunnel envelope.

Following flutter clearance, a series of control power measurement runs was conducted using the baseline, clean wing model. Wing bending and torsion moment data were measured for various control surface setting combinations using the TEO, TEI, and leading-edge outboard (LEO) control surfaces. Figure 14 depicts measured wing root bending moment as dynamic pressure increases for the baseline model when the LEO (+ up) or TEO (+ down) surface is individually deflected. TEO surface aeroelastic reversal occurs at approximately 68 psf dynamic pressure. Due to nonlinearities, the reversal dynamic pressure varies slightly as deflection is increased. As shown in Fig. 14, the LEO surface generates appreciable outboard control power. The LEO control power

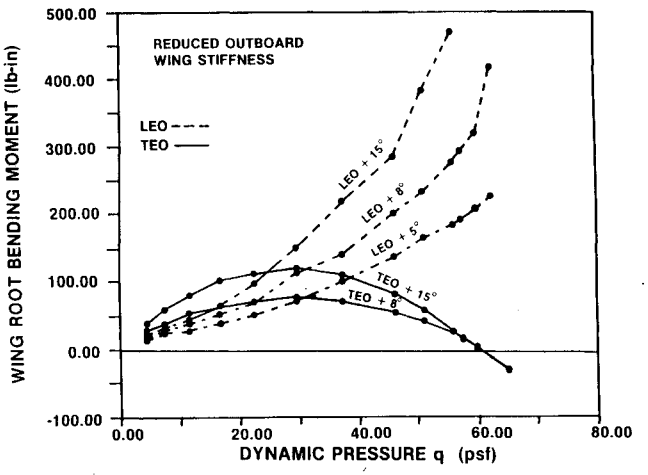

Fig. 15 Reduced stiffness wing root bending moments due to outboard surface deflection.

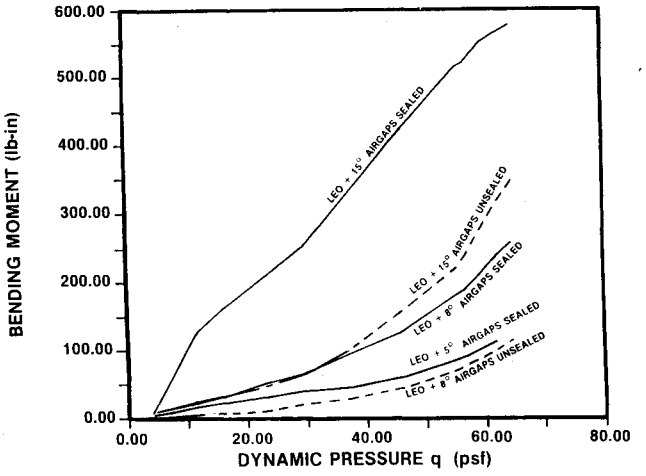

Fig. 16 Effect of sealing leading-edge control surface airgaps.

continually increases as dynamic pressure and surface deflection are increased.

A second flutter clearance run was conducted for the clean wing model configured with the reduced stiffness spar. The model was free from dynamic instabilities up to 70 psf dynamic pressure.

A second series of control power measurement runs was conducted for the model configured with the reduced stiffness spar. Figure 15 shows measured wing root bending moment as dynamic pressure increases for the reduced stiffness model when the LEO or TEO surface is individually deflected. The TEO surface reverses at approximately 61 psf, 10% lower than for the baseline spar. Net control power achieved through use of the TEO surface is also reduced. However, net LEO surface control power increases significantly over that achieved for the baseline configuration. A comparison of Figs. 14 and 15 reveals that as wing flexibility increases, the loss in TEO surface control power is traded for an increase in LEO surface control power. This loss in TEO surface power and increase in LEO surface power for the reduced stiffness model is due to the increased twisting of the wing sections due to reduced torsional stiffness.

A third series of runs was conducted to examine losses in LEO surface aerodynamic effectiveness caused by the unsealed airgaps between the model control surface sections. Figure 16 shows the additional bending moment generated using the baseline model when the leading-edge airgaps were sealed with tape. The trends clearly show significant aerodynamic losses. Sealing of airgaps was considered undesirable because sealants increase model stiffness and change frequency and damping characteristics. Therefore, the remaining data presented were obtained with the airgaps unsealed.

Wing roll derivatives were derived from test data for the baseline model LEO, TEO, and TEI surfaces. These derivatives are similar to the aircraft rolling moment coefficient $C_{l\delta}$ except the distance from the wing root to the fuselage centerline is neglected. Derivatives, at test point dynamic pressures, are equivalent to the slope of least square curve fits applied to nondimensionalized, incremental wing root bending moments plotted as a function of control surface deflection.

Figure 17 depicts the baseline wing moment derivatives plotted vs dynamic pressure. ASTROS code derivative predictions are also shown. The ASTROS predictions for the LEO surface correlated reasonably with measured data. Steady aerodynamic forces acting on the LEO surface were modeled with 100% aerodynamic effectiveness in the ASTROS model.

ASTROS prediction of the TEO surface aeroelastic reversal dynamic pressure fell within 2% of the measured value of 68 psf. To correlate with measured TEO surface derivatives, the steady, linear aerodynamic forces acting on the TEO surface in ASTROS had to be reduced 60% in effectiveness. Typical aerodynamic modeling losses for trailing-edge surfaces usually do not exceed 40%. However, an additional reduction in aerodynamic effectiveness in ASTROS was considered reasonable due to the presence of the air gaps on the model control surfaces.

A 136 psf TEI surface aeroelastic reversal dynamic pressure was found by extrapolation of the measured derivative trend. ASTROS prediction of the TEI surface aeroelastic reversal dynamic pressure fell within 2% of the extrapolated value. To be consistent, ASTROS steady aerodynamic forces acting on the TEI surface were also reduced by 60% in effectiveness. Predicted derivatives for the TEI surface were slightly low at lower dynamic pressures but were fairly reasonable at higher dynamic pressures.

Figure 18 compares control power generated in the form of wing root bending moment using the baseline and increased flexibility models. The moments were measured by deflecting

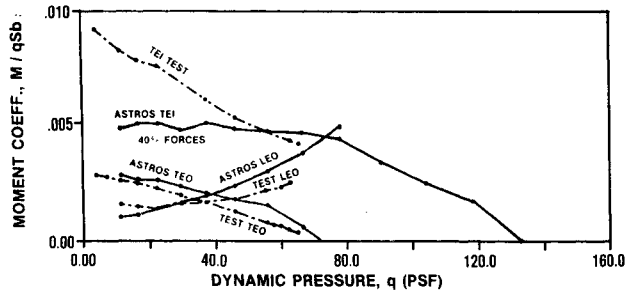

Fig. 17 Comparison of control surface moment derivatives.

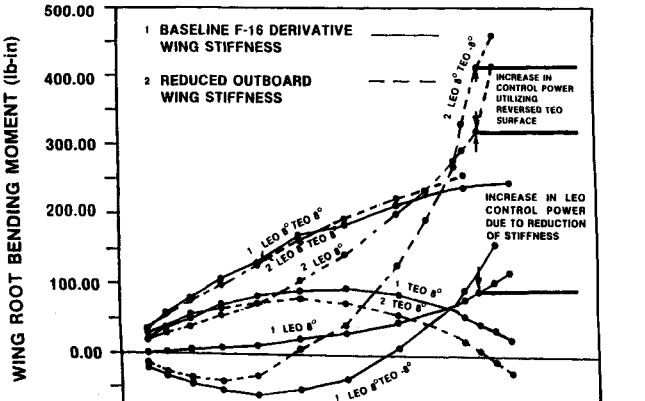

Fig. 18 Bending moment comparison of baseline and flexible wings outboard surfaces.

combinations of LEO and TEO surfaces to ±8 degrees. At lower dynamic pressures, positive deflection of both the LEO surface and the TEO surface result in the greatest available control power and differences between configurations is negligible. At high dynamic pressures, positive deflection of the LEO surface alone or in combination with negative deflection of the TEO surface generates greater control power for the more flexible wing. The data clearly show that the configuration with increased flexibility generates higher bending moments and corresponding control power at high dynamic pressure.

Conclusions

A precision, low-speed wind-tunnel model simulating a derivative wing for the U.S. Air Force F-16 fighter was designed, constructed, and tested in the wind tunnel. The model was equipped with multiple leading- and trailing-edge control surfaces. Static load test results approximated static load analyses of the full-scale design. Vibration test results and modal analyses for the model and full scale finite element model compared favorably.

The Active Flexible Wing concept was successfully applied to the F-16 derivative wing through the design, fabrication, and testing of a baseline and a reduced stiffness model. The leading-edge outboard surface proved to be effective for both configurations, but was particularly effective when used on the reduced stiffness wing. Near dynamic pressures where the baseline wing trailing-edge outboard (TEO) surface becomes ineffective due to wing flexibility, significant control power could be generated using the baseline wing leading-edge outboard (LEO) surface. Wind tunnel results showed that, by reducing the outboard wing stiffness 25%, control power generated at high dynamic pressures using the LEO surface exceeded that generated using the LEO surface on the baseline wing by a factor of two to four. By deflecting the reversed TEO surface opposite to conventional deflection, the control power, at high dynamic pressure, was increased approximately 10% above that generated using only the LEO surface.

Transonic and supersonic data from Ref. 1 shows that Mach effects nearly double the flexible effectiveness of the leading-edge control surface while trailing edge effectiveness and reversal speed are nearly halved. This trend suggests that the benefits of flexible wing technology are much greater than can be noted during subsonic testing, where only dynamic pressure effects can be addressed.

References

[1]Miller, G., "Active Flexible Wing (AFW) Technology," Air Force Wright Aeronautical Laboratories TR-87-3096, Feb. 1988.

[2]Pendleton, E., Lee, M., and Wasserman, L., "A Low Speed Flexible Model Simulating an F-16 Derivative Wing Design," Wright Research and Development Center TR-90-3083, Jan. 1991.

[3]Love, M., "General Dynamics Advanced Wing Data Package," March 1988.

[4]"The NASTRAN User's Manual," Level 17.5, *Cosmic*, University of Georgia, Athens, Georgia, Dec. 1978.

[5]Neill, D. J., Johnson, E. H., and Canfield, R., "ASTROS-A Multidisciplinary Automated Structural Design Tool," *Twenty-eighth Annual AIAA/American Society of Mechanical Engineers/American Society of Civil Engineers/American Helicopter Society Structures, Structural Dynamics and Materials Conference,* Monterey, CA, April 1987.

[6]Neill, D., Johnson, E., and Herendeen, D., "Automated Structural Optimization System (ASTROS)," Vol. II, User's Manual, Air Force Wright Aeronautical Laboraties TR-88-3028, April 1988.

[7]Smilg, B., and Wasserman, L., "Applications for Three Dimensional Flutter Theory of Aircraft Structures," Air Force Technical Report 4798, July 1942.

[8]Bisplinghoff, R., Ashley, H., and Halfman, R., "Aeroelasticity," Addison Wesley, Reading, MA, 1955.

[9]Roark, R. J., "Formulas for Stress and Strain," McGraw Hill, New York, 1965.

[10]Giesing, J. P., Kalman, T. P., and Rodden, W. P., "Subsonic Unsteady Aerodynamics for General Configurations," Air Force Flight Dynamics Laboratory TR-71-5, 1971.